CHEMISTRY OF MATERIALS

pubs.acs.org/cm

Article

Reentrant Negative Linear Compressibility in MIL-53(Al) over an Ultrawide Pressure Range

Dequan Jiang, Ting Wen,* Yanzhen Guo, Jie Liang, Zimin Jiang, Chen Li, Ke Liu, Wenge Yang, and Yonggang Wang*

Cite This: *Chem. Mater.* 2022, 34, 2764−2770

Read Online

HPSTAR 1579-2022

ACCESS | Metrics & More | Article Recommendations | Supporting Information

ABSTRACT: Anomalous compression behaviors such as negative linear compressibility (NLC) and negative area compressibility (NAC) are emerging functionalities essential for utilities under extreme conditions. Metal−organic frameworks (MOFs) present a large family of NLC/NAC materials under the well-recognized "wine-rack" mechanism. Nevertheless, the working pressure of MOFs is limited to typically no more than 3 GPa. Herein, we report the observation of a rare reentrant NLC behavior of MIL-53(Al) over an ultrawide pressure region up to 41.6 GPa. MIL-53(Al) with the classic wine-rack topology first exhibits an NLC behavior along the *c*-axis in the pressure region of 0−2.7 GPa, followed by a normal compression process between 2.7 and 12.9 GPa. After that, it is surprising to find that the reentrant NLC property remains at a record-high pressure (>40 GPa) among the previously reported MOFs. The mechanisms of the distinct compression behaviors of MIL-53(Al) in the three stages are studied by combining the X-ray diffraction analyses, Raman spectra, and DFT calculation. Particularly, the photoluminescence of Cr^{3+} is used as a unique probe for the subtle changes of the local coordination environments of Al^{3+} under compression. Both the absorption spectra and photoluminescence of Cr^{3+}-doped MIL-53(Al) not only verify the three-stage compression processes but also reveal a hidden structural/electrical phase transition around 22.0 GPa. These findings provide an in-depth understanding of the structure−property relationship of abnormal compression behavior at the local-structure level.

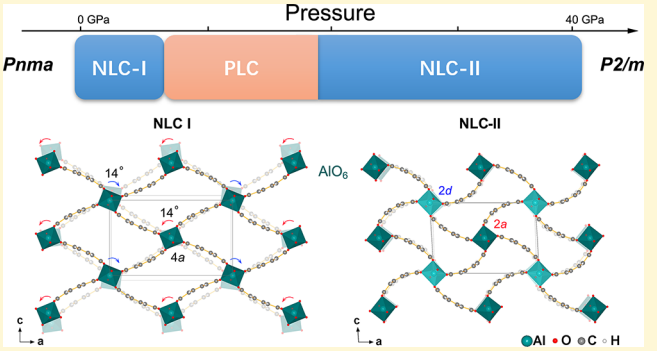

INTRODUCTION

Negative linear compressibility (NLC) is an anomalous mechanical behavior describing that a material can expand along a specific direction under uniform compression without any phase transition. NLC is thermodynamically allowed for it couples to the volume reduction but goes against the intuition that the compression is bound to generate the contraction.[1−3] NLC materials spur great interests in the exploration of inherent mechanisms for their unusual elasticity, which may also exploit a range of promising application fields such as interferometric pressure sensors, artificial muscles, and shock-resisted optical fibers.[4−6] Up to now, the NLC phenomenon has been observed in a diversity of materials, involving inorganic compounds such as BPO_4, $BAsO_4$, and α-BiB_3O_6, and metal−organic frameworks (MOFs) such as $Ag_3[Co(CN)_6]$, $Zn[Au(CN)_2]_2$, and $KMn[Ag(CN)_2]_3$.[7−12] Several kinds of mechanisms for the generation of NLC have been proposed for specific materials, such as wine-rack and honeycomb networks, and the Lifshitz model.[11−14]

MOFs are compounds with framework architectures constructed by metal ions or clusters (nodes) and organic linkers (struts).[15,16] MOFs always show considerable structural flexibility in response to pressure, such as NLC, symmetry-lowering, and amorphization, owing to the polyhedron rotation or framework relaxation.[8,17−19] Particularly, when structural phase transition occurs along with an NLC behavior, a two-stage NLC phenomenon may be observed in both the low-pressure (LP) and high-pressure (HP) phases with a closely related mechanism. These reported examples include $Ag_3[Co(CN)_6]$ (phase I: K_c = −76 TPa^{-1}, 0−0.19 GPa; phase II: K_c = −5.3 TPa^{-1}, 0.19−7.65 GPa) and $Zn[Au(CN)_2]$ (phase I: K_c = −42 TPa^{-1}, 0−1.8 GPa; phase II: K_c = −5.3 TPa^{-1}, 1.8−14.2 GPa).[10,12] Also, owing to the structural flexibility, NLC within MOFs is usually restricted to very low pressures, after which the pressure-driven structural phase transition or amorphization possibly occurs with the disappearance of NLC.[19] The strategy of inclusion of counterions within the framework

Received: December 22, 2021
Revised: February 9, 2022
Published: February 21, 2022

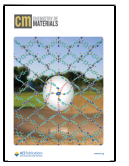

https://doi.org/10.1021/acs.chemmater.1c04398
Chem. Mater. 2022, 34, 2764−2770

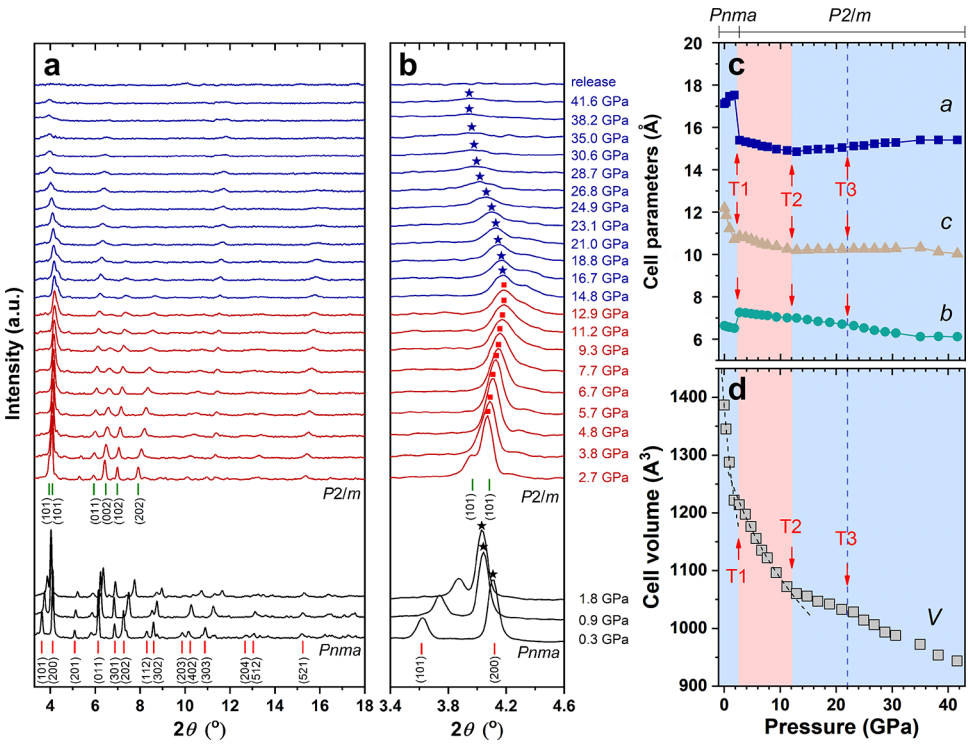

Figure 1. XRD patterns reveal the reentrant NLC behavior of MIL-53(Al). (a) Powder XRD patterns of MIL-53(Al) as a function of pressure. (b) Enlarged XRD patterns in the 2θ range of 3.4° to 4.6°. (c) Cell parameters of MIL-53(Al) as a function of applied pressure. (d) Cell volumes as a function of applied pressure. $P-V$ fitting results: phase I: V_0 = 1382.8 ± 3.2 Å, B_0 = 11.3 ± 0.4 GPa, B' = 4; phase II: V_0 = 1292.2 ± 4.2 Å, B_0 = 41.0 ± 1.3 GPa, B' = 4.

cavities is used to extend the NLC pressure range. However, the highest NLC pressure is no more than 15 GPa in all the ever reported MOFs, which is much lower than that of the inorganic NLC materials and limits the potential applications of NLC MOFs.[8,20,21]

With the purpose of exploring NLC MOFs that can survive to a higher pressure range, we have screened dozens of known MOFs under compression. Among them, MIL-53 is of a representative wine-rack topology, where the metal-centered octahedra locate the vertexes as hinges and are bridged by the organic ligands.[22] The NLC behavior of MIL-53(Al)-lp has been reported in 2015, with a compressibility value of −28 TPa^{-1} within 0−3 GPa along the *a*-axis, positive contractions along all axes within 3−6 GPa, and no data for higher pressure.[23] Herein, we report the experimental data of MIL-53(Al) up to more than 40 GPa. Surprisingly, a rare reentrant NLC behavior has been observed in the 12.9−41.6 GPa region for the first time besides the previously reported NLC behavior in the LP range. Structural analyses based on in situ X-ray diffraction data and Raman spectra have been conducted to reveal the structure evolution through the NLC within different pressure ranges. Particularly, the photoluminescence (PL) of Cr^{3+} is used as a unique probe for the subtle changes of the local coordination environments of Al^{3+} under compression. Dramatic changes of the optical properties in Cr^{3+}-doped MIL-53(Al) were observed and corresponded well to the NLC behavior and pressure-induced structure transitions.

EXPERIMENTAL DETAILS

Material Synthesis. Polycrystalline samples of MIL-53(Al) were synthesized following the reported method.[22] Aluminum nitrate nonahydrate ($Al(NO_3)_3{\cdot}9H_2O$, Aladdin, 99%), terephthalic acid ($C_8H_6O_4$, Aladdin, 99%), and deionized water were mixed at a molar ratio of 1:0.5:80 and then reacted under a hydrothermal condition of 220 °C for 72 h. The product was collected after washing with deionized water/ethanol and drying at 80 °C overnight. For 5% Cr^{3+}-doped MIL-53(Al), chromium(III) nitrate nonahydrate ($Cr(NO_3)_3{\cdot}9H_2O$, Aladdin, 99%) was added into the reactant instead of 5 mol % $Al(NO_3)_3{\cdot}9H_2O$.

Characterizations under Ambient Conditions. The phase purity of the as-obtained MIL-53 (Al):5% Cr was analyzed by using a PANalytical Empyrean diffractometer (Cu Kα source (λ = 0.154 nm)), and the absorption spectra of the 5% Cr^{3+}-doped MIL-53(Al) powder were measured by a UV−Vis spectrophotometer (U-4100, Hitachi) with an integrating sphere.

In Situ HP Characterizations. Standard symmetrical diamond anvil cells (DACs) with 300 μm culets were used in all HP measurements. Stainless steel or rhenium gaskets were pre-indented to about 40 μm in thickness, and 150 μm holes were drilled using a laser drilling system to serve as the sample chambers. The sample powder was pressed into a pellet and loaded into the sample chamber filled with silicone oil as the pressure-transmitting medium (PTM). A ruby sphere was then loaded to calibrate the pressure by using the ruby fluorescence method.[24]

HP powder X-ray diffraction (XRD) patterns were collected at the 4W2 High Pressure Station in Beijing Synchrotron Radiation Facility (BSRF). A focused monochromatic X-ray beam with a size of about 15 × 35 μm^2 and a wavelength of 0.6199 Å was used. The diffraction data were recorded by the Mar345 image plate. High-purity CeO_2 powder was used as the standard for calibration. The powder XRD patterns were integrated with the Dioptas program.[25] Lattice parameter refinements were performed by using the FULLPROF program.[26] The compressibility was calculated by the empirical function $l = l_0 + \lambda(p - p_c)^n$ via the online program PASCal (http://pascal.chem.ox.ac.uk/).[27]

The HP Raman spectra were collected using a 532 nm line and a 2400 slits/mm diffraction grating in a Renishaw inVia spectrometer.

https://doi.org/10.1021/acs.chemmater.1c04398
Chem. Mater. 2022, 34, 2764−2770

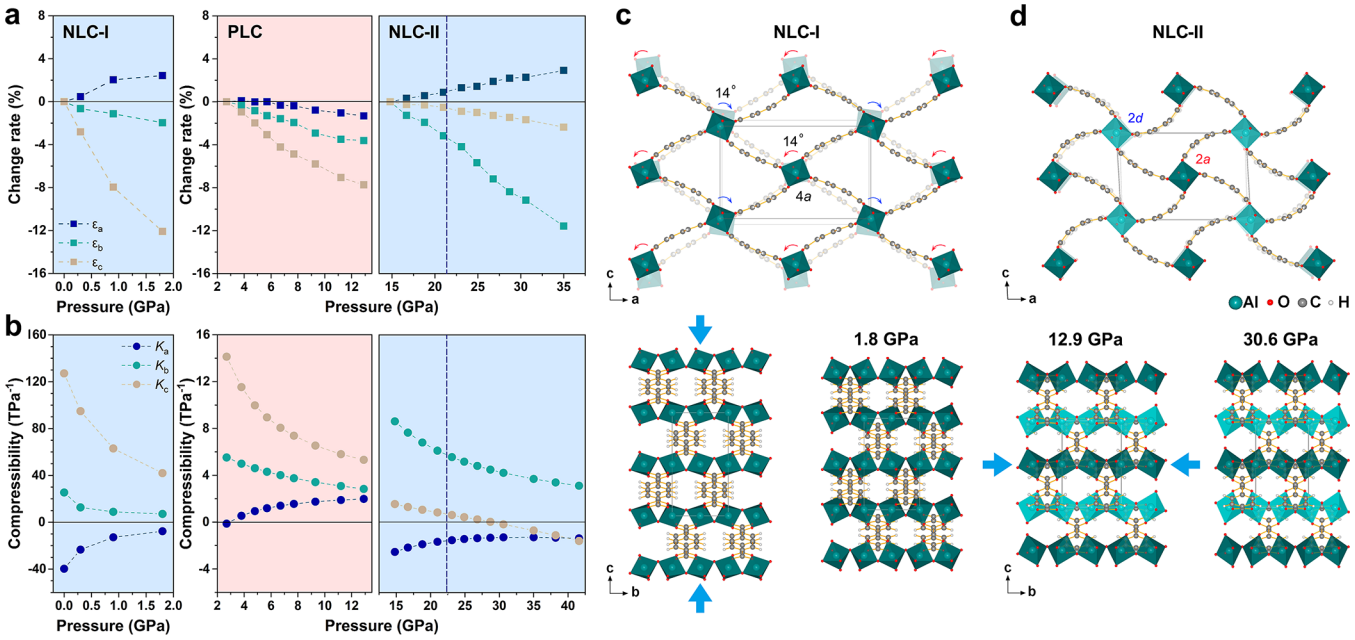

Figure 2. Reentrant NLC behavior of MIL-53(Al) and its structural origination. (a) Change rate of the lattice parameters as a function of pressure. (b) Compressibility coefficients of the lattice parameters as a function of pressure. (c, d) Schematic representations of the framework evolution of MIL-53(Al) during **NLC-I** and **NLC-II**.

HP UV−Vis absorption spectrum measurements were conducted using an Ocean Optics QE65000 scientific-grade spectrometer. In situ HP PL spectrum measurements were conducted by using a home-designed spectroscopy system (Ideaoptics, Shanghai, China) with a 405 nm laser as the excitation light source. The bandgap value was derived from the optical absorbance data by using the Tauc plot method[28,29] according to the following equation:

$$(h\nu\alpha)^{1/n} = A(h\nu - E_g)$$

where h is Planck's constant, ν is the frequency of vibration, α is the absorption coefficient, E_g is the bandgap, and A is the proportional constant. The value of the exponent n denotes the nature of the sample transition and is theoretically equal to 1/2 or 2 for direct allowed and indirect allowed transitions, respectively. For the sample of 5% Cr^{3+}-doped MIL-53(Al), the value of n was selected to be 1/2.

The first-principles calculation was performed using the CASTEP package.[30] The ambient crystal structure of MIL-53(Al) was adopted as the initial structure model. Structure optimization at various pressure points was performed adopting the experimental cell sizes with all the atomic positions relaxed. The electron−electron interaction was treated with an energy cutoff of 600 eV using the LDA and PAW−PBE pseudopotential. The valance electrons of H, C, O, and Al were $1s^1$, $2s^22p^2$, $2s^22p^4$, and $3s^23p^1$, respectively.

RESULTS AND DISCUSSION

The Pressure-Driven Structural Evolution of MIL-53(Al). Phase-pure polycrystalline samples of MIL-53(Al) and 5% Cr^{3+}-doped MIL-53(Al) were synthesized under the hydrothermal condition[22] (Figures S1 and S2). Figure 1 displays the in situ powder XRD patterns of MIL-53(Al) under the HP of up to 41.6 GPa. At ambient pressure, the diffraction peaks can be well indexed with the orthorhombic space group *Pnma*. In the representative XRD patterns between 3.4° and 4.6°, the diffraction peak (200) shifts to lower angles before 1.8 GPa (**NLC-I**), indicating that abnormal enlargement of the *d*-spacing of (200) occurs upon compression. Visual evidence can be found with the shift of (101) and (200) peaks in the raw two-dimensional XRD images (Figure S3). As the pressure increased sequentially, the (101) and (200) peaks merge together and shift toward the high-angle region. A structural phase transition occurs around 2.7 GPa from orthorhombic to monoclinic ($P2/m$) according to the Le Bail fitting results (Figure S4). No evident structural phase transition has been observed from the diffraction data up to 41.6 GPa. Surprisingly, the XRD peak around 4° moves toward a high angle first in the 2.7−12.9 GPa region (positive linear compressibility, **PLC**) and then to a low-angle direction again above 12.9 GPa (**NLC-II**), indicating the reentrant NLC behavior. MIL-53(Al) suffers an irreversible pressure-induced amorphization at the higher pressure region around 40 GPa and after releasing to ambient conditions. Figure 1c,d shows the lattice parameters extracted from the refinement of the XRD data. Three pressure points, namely, **T1**, **T2**, and **T3**, are marked to show either the structural transitions or electrical transition evidenced by the PL property. **T1** at 2.7 GPa marks the transformation from orthorhombic to monoclinic phase (*Pnma* to $P2/m$) and also from NLC to PLC along the *a*-axis. The second transition occurred at 12.9 GPa (**T2**), followed by the reentrant NLC behavior in MIL-53(Al) along the *a*-axis. **T3** labels the anomalous compressibility of the cell volume, which has been confirmed by the anomalous change of the PL property (will be discussed in the optical property section).

NLC Property of MIL-53(Al). "Reentrant" phenomena are rare but extremely important to understand the essence of critical physical behaviors such as orbital ordering, magnetic frustration, and lattice expansion.[31−34] From the cell parameter evolution as a function of pressure, we notice that MIL-53(Al) expands again along the *a*-axis above 12.9 GPa besides the **NLC-I** region, which presents an emerging "reentrant" NLC phenomenon among all the previously reported NLC materials. Figure 2 shows the pressure-dependent change and compressibility coefficients of the lattice parameters during both the **NLC-I** and **NLC-II** processes. In the first stage at 0−1.8 GPa, the framework of MIL-53(Al) extends by 2.4% along the *a*-axis and contracts by 12.1% in the *c* direction, much

https://doi.org/10.1021/acs.chemmater.1c04398
Chem. Mater. 2022, 34, 2764−2770

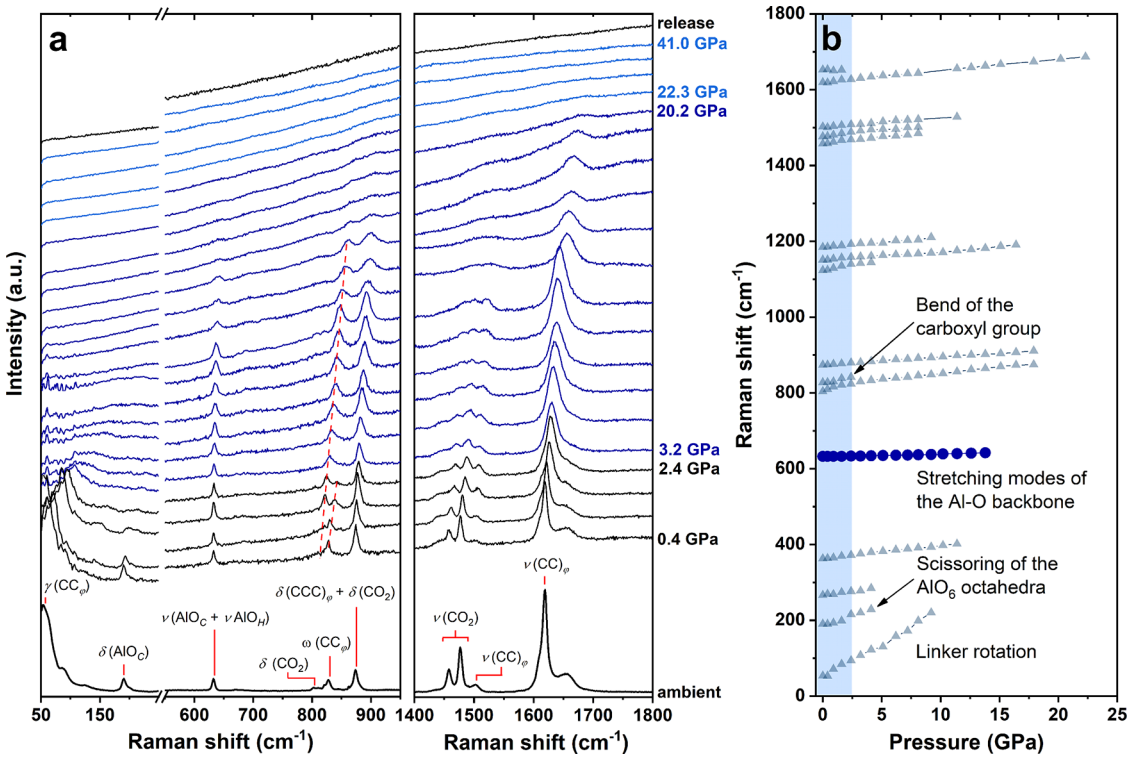

Figure 3. Raman evidence for the NLC mechanism in MIL-53(Al). (a) Raw Raman spectra for MIL-53(Al) as a function of pressure. (b) Pressure dependence of the Raman peak locations of MIL-53(Al).

bigger than that along the *b*-axis (by 2.0%). The compressibility coefficients of the three unit-cell axes are calculated by using the PASCal program,[27] which gives the values of K_a = −7.7 TPa^{-1}, K_b = 7.1 TPa^{-1}, and K_c = 41.9 TPa^{-1}. Compared with the previously reported MIL-53(Al)-lp (K_b = −28 TPa^{-1}),[23] the NLC value along the *a*-axis (−7.7 TPa^{-1}) is much smaller, which can be attributed to the filled holes of MIL-53(Al) by the ligand molecules resistant to external pressure. The **NLC-II** stage occurs in the pressure range of 12.9−41.6 GPa, where the *a*-axis elongates by 3.3% and the *b*-axis compresses by 12.5%, compared with that along the *c*-axis by about 3%. The corresponding compressibility coefficients are K_a = −1.3 TPa^{-1}, K_b = 0.6 TPa^{-1}, and K_c = 0.3 TPa^{-1}, respectively. Compared with the other NLC materials including MOFs, the compressibility along the *a*-axis in **NLC-II** is quite smaller, but the pressure range with NLC is the largest up to now (Table S1). Normally, almost all of the materials with abnormal compressibility that can survive to a relatively high pressure (several tens of GPa) are all inorganic materials, such as BPO_4 and $BAsO_4$.[8]

The structure evolution of MIL-53(Al) under compression is evaluated by DFT structure optimization using the experimental cell parameters at given pressures. Under ambient conditions, the corner-sharing AlO_6 octahedra bridged by the terephthalic acid ligands arrange along the *b*-axis, with all the Al atoms occupying the 4*a* position. In the **NLC-I** stage, the column of AlO_6 octahedra falls into two categories and rotate in opposite directions around the *b*-axis (about 14°), making the framework prolonged along the *a*-axis and contracted in both directions of the *b*, *c*-axis. This also creates two kinds of Al sites: 2*a* (Al1) and 2*d* (Al2), which breaks the crystalline symmetry into the space group *P*2/*m*. With the rotation of AlO_6 octahedra, the organic ligands bend slightly on the joint between the benzene ring and the $-CO_2-$ group.[35−37] Similar phase transition has been reported in $Zn(CN)_2$ initialed by the rotations of the polyhedra in the opposite directions.[38] In the **NLC-II** stage, the shrinkage of the Al−O−Al angles turns into the most likely mechanism for the *a*-axis stretching instead of the rotations of the octahedra (Table S2). The Al−O−Al angles decrease by about 10°, which is nearly 10 times larger than that in the **NLC-I** stage. As a result, the *b*-axis has a bigger magnitude of compression in the **NLC-II** process instead of the *c*-axis in the **NLC-I** stage.

Raman Evidence for the NLC Mechanism. Raman measurements are conducted to probe into the subtle local structure evolution of MIL-53(Al) under compression. Figure 3 shows the representative Raman spectra recorded in the 50−1800 cm^{-1} region of up to 41.6 GPa. The first stage falls into the pressure range below 2.4 GPa, coinciding with the structural phase transition point **T1** as evidenced by the XRD results. In this range, the peak at 54 cm^{-1} weakened sharply, which can be attributed to the depressed rotation of the phenyl in the framework by pressurization (Table S3). The peak at 184 cm^{-1} is assigned to the scissoring-like bending of the AlO_6 octahedra, which disappears at 2.4 GPa. The scissoring of the AlO_6 octahedra is linked with a seesaw motion of the phenyl, which is considered one of the triggering factors for the breathing of MIL-53(Al).[39] The weakening of this Raman peak therefore indicates that the motion of the skeleton associated with "breathing mode" is restrained at a fairly low pressure. The peak located at 827 cm^{-1} is ascribed to the out-of-plane waggling vibration between the carbon atoms and the aromatic rings, which decreases and finally vanishes at 2.4 GPa. Meanwhile, the peak at 804 cm^{-1} relative to the bending vibration of −O−C−O− groups increases upon compression, which strongly indicates the pressure-induced bending between $-CO_2-$ groups and aromatic rings. All evidence confirms the structural evolution of the MIL-53(Al)

https://doi.org/10.1021/acs.chemmater.1c04398
Chem. Mater. 2022, 34, 2764−2770

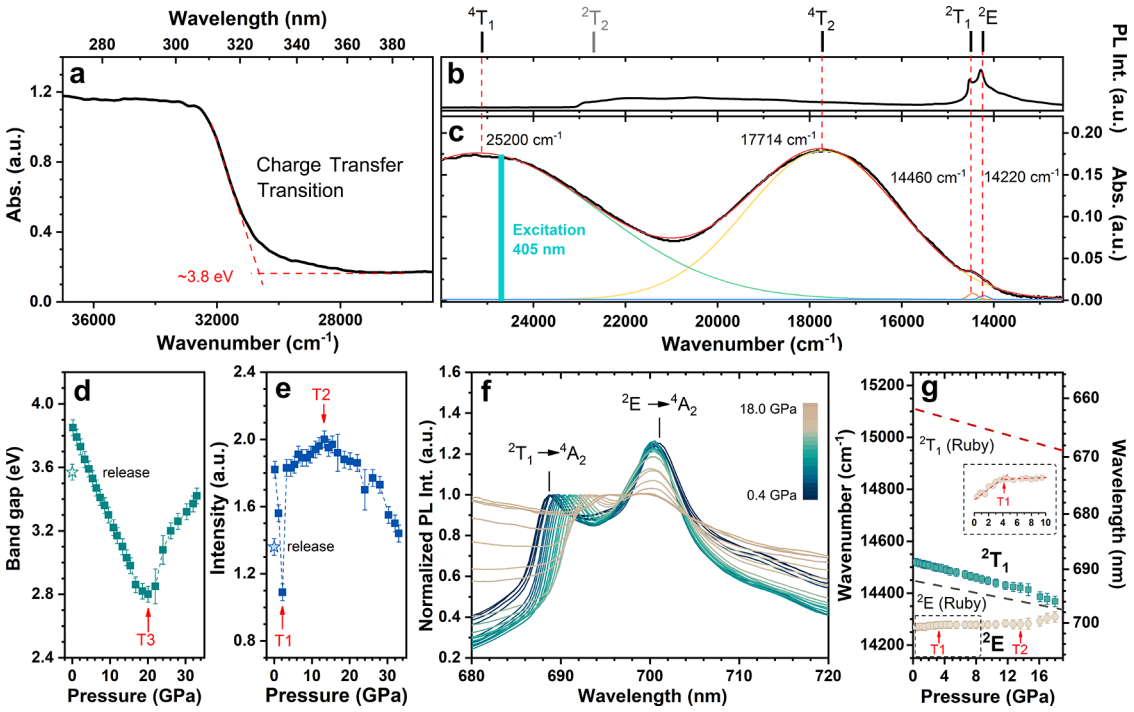

Figure 4. Optical spectra of 5% Cr^{3+}-doped MIL-53(Al) under compression. (a) Optical absorption edge of 5% Cr^{3+}-doped MIL-53(Al) in the range of 25,000−37,000 cm^{-1}. (b) PL spectrum of 5% Cr^{3+}-doped MIL-53(Al) excited by a 405 nm laser. (c) Absorption spectrum of the d−d transitions of 5% Cr^{3+}-doped MIL-53(Al). (d) Bandgap evolution of 5% Cr^{3+}-doped MIL-53(Al) as a function of pressure. (e) Intensity of CT absorption as a function of pressure. (f) PL spectra of Cr^{3+} ions in 5% Cr^{3+}-doped MIL-53(Al) as a function of pressure. (g) Energy levels of Cr^{3+} in 5% Cr^{3+}-doped MIL-53(Al) as a function of pressure, compared with those in ruby (Cr^{3+}-bearing Al_2O_3).[40]

framework under high pressure and supports the previously proposed NLC mechanism.

As pressure increases continually, all the Raman peaks decrease gradually and disappear around 20 GPa, corresponding to the transition point **T3** and the irreversible amorphization from the XRD results. Notably, the Raman peak around 632 cm^{-1} corresponding to the stretching mode of the Al−O backbone basically remains unshifted in the whole compression process, which shows the stiffness of the AlO_6 octahedra when put together with organic linkers. This phenomenon can also support the abovementioned NLC mechanism and the structural evolution of MIL-53(Al) under compression.

Cr^{3+} Optical Probe for the NLC Mechanism of MIL-53(Al). Optical signals have always been used as sensitive probes to detect subtle local structure changes of materials responsive to external stimuli.[41,42] The emission bands of Cr^{3+} are adopted to get deep insights into the local structure change of MIL-53(Al) under compression. The Cr^{3+} ions with $3d^3$-configuration are centered at distorted octahedral sites with O^{2-} ions occupying the vertices in Cr^{3+}-doped MIL-53(Al), where the electronic energy levels of Cr^{3+} ions can be well described by the ligand-field theory. The octahedral field gives rise to the split d-electron levels of Cr^{3+} ions, and the reduced site symmetry caused by the distortion of the octahedron leads to partial removal of the electronic degeneracies.[43,44] Thus, the migration of ion energy levels can give an index to the change of the local lattice structure. Figure 4 shows the optical spectra (absorption and emission) of 5% Cr^{3+}-doped MIL-53(Al) under ambient conditions and under compression. First, the absorption and emission spectra of 5% Cr^{3+}-doped MIL-53(Al) powder were measured under ambient conditions to confirm the energy level structure of the Cr^{3+} ion. A strong absorption band appeared at the high frequency region, above 31,000 cm^{-1}, which can be assigned to the charge transfer (CT) transition. The emission spectrum (excited by a 405 nm laser) coupled with the absorption spectrum was utilized for the clarification of the d−d transition energy levels. The broad bands centered at 25,200 and 17,714 cm^{-1} can be ascribed to the transitions of $^4A_2 \rightarrow {}^4T_1$ and $^4A_2 \rightarrow {}^4T_2$, respectively. In contrast to the location of emission peaks, the small absorption peak at the low frequency region was separated into two peaks centered at 14,460 and 14,220 cm^{-1}, assigned to the transitions of $^4A_2 \rightarrow {}^2T_1$ and $^4A_2 \rightarrow {}^2E$, respectively. The value of the $^2T_2$ energy level was calculated by using the spectral data according to the ligand-field theory and put at 23,700 cm^{-1}.[45]

Under compression, the bandgap (calculated from the absorption edge, Figures S5 and S6) and the emission from transitions of $^2T_1 \rightarrow {}^4A_2$ and $^2E \rightarrow {}^4A_2$ were measured and analyzed together with structural evolution concluded from XRD patterns. The bandgap values decreased from 3.85 eV under ambient conditions to 2.8 eV at ∼20 GPa and then continued to increase to 3.42 eV around 33 GPa. After the pressure was released, this value reached 3.57 eV. The inflection that appeared at ∼20 GPa corresponds roughly to the transition point **T3** as evidenced from the XRD and Raman measurements. In addition, the CT absorption intensity shows several discontinuities under compression, corresponding to the **T1** and **T2** transitions at 2.2 and 13.3 GPa, respectively. All the abrupt changes arising in the evolution of absorption properties provide strong evidence for the phase transition during pressurization. These two changes can also be found in the PL emission peak shifts under compression (Figure 4f,g). It is interesting to find a red-shift of the $^2T_1 \rightarrow {}^4A_2$ peak and a

https://doi.org/10.1021/acs.chemmater.1c04398
Chem. Mater. 2022, 34, 2764−2770

slight blue-shift of the $^2E \rightarrow {}^4A_2$ peak under compression. Two inflection points are observed at 4.2 and 13.6 GPa, consistent with the abovementioned phase transitions **T1** and **T2**. Remarkably, it is unusual to see a blue-shift of the $^2E \rightarrow {}^4A_2$ transition under compression compared to that in Cr^{3+}-bearing ruby that served as a widely used pressure gauge.[40] The opposite PL shift is just unique evidence supporting the anomalous NLC behavior of MIL-53(Al).

CONCLUSIONS

In summary, we report a reentrant NLC behavior of MIL-53 (Al) that can survive up to more than 40 GPa. Three distinct compression regions are observed: **NLC-I**, 0−2.7 GPa, with the wine-rack mechanism; **PLC**, 2.7−12.9 GPa, with normal compression behavior; **NLC-II**, 12.9−41.6 GPa, with a complex rotation mechanism. Local structure analyses based on Raman spectral evidence strongly support the distinct NLC mechanisms in the **NLC-I** and **NLC-II** stages. The Cr^{3+} optical properties (absorption and emission) are first used as sensitive structure probes into the subtle coordination changes of the AlO_6 octahedra and provide consistent results with the structural characterizations. The discovery of a reentrant NLC behavior in a given material and an NLC that can survive to ultrahigh pressure in a soft MOF provides a state-of-the-art platform for the study and rational design of more materials with abnormal compressibility.

ASSOCIATED CONTENT

Supporting Information

The Supporting Information is available free of charge at https://pubs.acs.org/doi/10.1021/acs.chemmater.1c04398.

Additional measurement results, including the XRD patterns and EDS results of MIL-53(Al) and 5% Cr^{3+}-doped MIL-53(Al), two-dimensional raw XRD images, Le Bail refinement results of the LP and HP phases, and in situ absorption spectra of 5% Cr^{3+}-doped MIL-53(Al) (PDF)

AUTHOR INFORMATION

Corresponding Authors

Ting Wen − *Center for High Pressure Science and Technology Advanced Research (HPSTAR), Beijing 100094, China;* orcid.org/0000-0001-6572-0920; Email: ting.wen@hpstar.ac.cn

Yonggang Wang − *Center for High Pressure Science and Technology Advanced Research (HPSTAR), Beijing 100094, China;* orcid.org/0000-0003-4816-9182; Email: yonggang.wang@hpstar.ac.cn

Authors

Dequan Jiang − *Center for High Pressure Science and Technology Advanced Research (HPSTAR), Beijing 100094, China;* orcid.org/0000-0003-0998-5507

Yanzhen Guo − *Institute of Nanostructured Functional Materials, Huanghe Science and Technology College, Zhengzhou, Henan 450006, China*

Jie Liang − *School of Energy and Power Engineering, Beihang University, Beijing 102206, China;* orcid.org/0000-0001-6305-8056

Zimin Jiang − *Center for High Pressure Science and Technology Advanced Research (HPSTAR), Beijing 100094, China*

Chen Li − *Center for High Pressure Science and Technology Advanced Research (HPSTAR), Beijing 100094, China*

Ke Liu − *Center for High Pressure Science and Technology Advanced Research (HPSTAR), Beijing 100094, China*

Wenge Yang − *Center for High Pressure Science and Technology Advanced Research (HPSTAR), Beijing 100094, China*

Complete contact information is available at: https://pubs.acs.org/10.1021/acs.chemmater.1c04398

Notes

The authors declare no competing financial interest.

ACKNOWLEDGMENTS

This work was supported by the Major Program of National Natural Science Foundation of China (22090041), National Natural Science Foundation of China (52073003), and National Key R&D Program of China (2018YFA0305900). The HP XRD data were collected at the 4W2 High Pressure Station in the Beijing Synchrotron Radiation Facility (BSRF).

REFERENCES

(1) Jiang, X.; Molokeev, M. S.; Dong, L.; Dong, Z.; Wang, N.; Kang, L.; Li, X.; Li, Y.; Tian, C.; Peng, S.; Li, W.; Lin, Z. Anomalous mechanical materials squeezing three-dimensional volume compressibility into one dimension. *Nature Commun.* **2020**, *11*, 5593−5599.

(2) Zeng, Q.; Wang, K.; Zou, B. Negative linear compressibility response to pressure in multitype wine-rack metal-organic frameworks. *ACS Mater. Lett.* **2020**, *2*, 291−295.

(3) Baughman, R.; Stafstrom, S.; Cui, C.; Dantas, S. Materials with negative compressibilities in one or more dimensions. *Science* **1998**, *279*, 1522−1524.

(4) Cairns, A. B.; Catafesta, J.; Hermet, P.; Rouquette, J.; Levelut, C.; Maurin, D.; Lee, A.; Dmitriev, V.; Bantignies, J.-L.; Goodwin, A. L.; et al. Effect of extra-framework cations on negative linear compressibility and high-pressure phase transitions: a study of $KCd[Ag(CN)_2]_3$. *J. Phys. Chem. C* **2020**, *124*, 6896−6906.

(5) Baughman, R. H. Auxetic materials: avoiding the shrink. *Nature* **2003**, *425*, 667−667.

(6) Aliev, A. E.; Oh, J.; Kozlov, M. E.; Kuznetsov, A. A.; Fang, S.; Fonseca, A. F.; Ovalle, R.; Lima, M. D.; Haque, M. H.; Gartstein, Y. N.; Zhang, M.; Zakhidov, A. A.; Baughman, R. H. Giant-stroke, superelastic carbon nanotube aerogel Muscles. *Science* **2009**, *323*, 1575−1578.

(7) Kobayashi, Y.; Deguchi, K.; Azuma, S.; Suzuki, E.; Ming, L. C.; Endo, S.; Kikegawa, T. Phase transitions in CsH_2PO_4 under high pressure. *Ferroelectrics* **2003**, *285*, 83−89.

(8) Kang, L.; Jiang, X.; Luo, S.; Gong, P.; Li, W.; Wu, X.; Li, Y.; Li, X.; Chen, C.; Lin, Z. Negative linear compressibility in a crystal of α-BiB_3O_6. *Sci. Rep.* **2015**, *5*, 13432−13438.

(9) Cairns, A. B.; Thompson, A. L.; Tucker, M. G.; Haines, J.; Goodwin, A. L. Rational design of materials with extreme negative compressibility: selective soft-mode frustration in $KMn[Ag(CN)_2]_3$. *J. Am. Chem. Soc.* **2012**, *134*, 4454−4456.

(10) Cairns, A. B.; Catafesta, J.; Levelut, C.; Rouquette, J.; Lee, A.; Peters, L.; Thompson, A. L.; Dmitriev, V.; Haines, J.; Goodwin, A. L. Giant negative linear compressibility in zinc dicyanoaurate. *Nat. Mater.* **2013**, *12*, 212−216.

(11) Cairns, A. B.; Goodwin, A. L. Negative linear compressibility. *Phys. Chem. Chem. Phys.* **2015**, *17*, 20449−20465.

(12) Goodwin, A. L.; Keen, D. A.; Tucker, M. G. Large negative linear compressibility of $Ag_3[Co(CN)_6]$. *Proc. Natl. Acad. Sci. U. S. A.* **2008**, *105*, 18708−18713.

(13) Jiang, X.; Luo, S.; Kang, L.; Gong, P.; Yao, W.; Huang, H.; Li, W.; Huang, R.; Wang, W.; Li, Y.; et al. Isotropic negative area compressibility over large pressure range in potassium beryllium

fluoroborate and its potential applications in deep ultraviolet region. *Adv. Mater.* **2015**, *27*, 4851−4857.
(14) Hodgson, S. A.; Adamson, J.; Hunt, S. J.; Cliffe, M. J.; Cairns, A. B.; Thompson, A. L.; Tucker, M. G.; Funnella, N. P.; Goodwin, A. L. Negative area compressibility in silver(I) tricyanomethanide. *Chem. Commun.* **2014**, *50*, 5264−5266.
(15) McKellar, S. C.; Moggach, S. A. Structural studies of metal-organic frameworks under high pressure. *Acta Cryst.* **2015**, *B71*, 587−607.
(16) Gagnon, K. J.; Beavers, C. M.; Clearfield, A. MOFs under pressure: the reversible compression of a single crystal. *J. Am. Chem. Soc.* **2013**, *135*, 1252−1255.
(17) Yu, Y.; Zeng, Q.; Chen, Y.; Jiang, L.; Wang, K.; Zou, B. Extraordinarily persistent zero linear compressibility in metal-organic framework MIL-122(In). *ACS Materials Lett.* **2020**, *2*, 519−523.
(18) Li, W.; Probert, M. R.; Kosa, M.; Bennett, T. D.; Thirumurugan, A.; Burwood, R. P.; Parinello, M.; Howard, J. A. K.; Cheetham, A. K. Negative linear compressibility of a metal-organic framework. *J. Am. Chem. Soc.* **2012**, *134*, 11940−11943.
(19) Collings, I. E.; Goodwin, A. L. Metal-organic frameworks under pressure. *J. Appl. Phys.* **2019**, *126*, 181101.
(20) Kamali, K.; Ravi, C.; Ravindran, T. R.; Sarguna, R. M.; Sairam, T. N.; Kaur, G. Linear compressibility and thermal expansion of $KMn[Ag(CN)_2]_3$ studied by Raman spectroscopy and first-principles calculations. *J. Phys. Chem. C* **2013**, *117*, 25704−25713.
(21) Marmier, A.; Ntoahae, P. S.; Ngoepe, P. E.; Pettifor, D. G.; Parker, S. C. Negative compressibility in platinum sulfide using density-functional theory. *Phys. Rev. B* **2010**, *81*, 172102.
(22) Loiseau, T.; Serre, C.; Huguenard, C.; Fink, G.; Taulelle, F.; Henry, M.; Bataille, T.; Férey, G. A rationale for the large breathing of the porous aluminum terephthalate, (MIL-53) upon hydration. *Chem. − Eur. J.* **2004**, *10*, 1373−1382.
(23) Serra-Crespo, P.; Dikhtiarenko, A.; Stavitski, E.; Juan-Alcañiz, J.; Kapteijn, F.; Coudertc, F.-X.; Gascon, J. Experimental evidence of negative linear compressibility in the MIL-53 metal-organic framework family. *CrystEngComm* **2015**, *17*, 276−280.
(24) Mao, H. K.; Xu, J.; Bell, P. M. Calibration of the ruby pressure gauge to 800 kbar under quasi-hydrostatic conditions. *J. Geophys. Res.* **1986**, *91*, 4673−4676.
(25) Prescher, C.; Prakapenka, V. B. DIOPTAS: a program for reduction of two-dimensional X-ray diffraction data and data exploration. *High Pressure Res.* **2015**, *35*, 223−230.
(26) Rodriguez-Carvajal, J. Recent advances in magnetic structure determination by neutron powder diffraction. *Physica B Condens. Matter* **1993**, *192*, 55−69.
(27) Cliffe, M. J.; Goodwin, A. L. PASCal: a principal axis strain calculator for thermal expansion and compressibility determination. *J. Appl. Crystallogr.* **2012**, *45*, 1321−1329.
(28) Tauc, J.; Grigorovici, R.; Vancu, A. Optical Properties and Electronic Structure of Amorphous Germanium. *Phys. Status Solid B* **1966**, *15*, 627−637.
(29) Davis, E. A.; Mott, N. F. Conduction in Non-crystalline Systems V. Conductivity, Optical Absorption and Photoconductivity in Amorphous Semiconductors. *Philos. Mag.* **1970**, *22*, 903−922.
(30) Clark, S. J.; Segall, M. D.; Pickard, C. J.; Hasnip, P. J.; Probert, M. J.; Refson, K.; Payne, M. C. First principles methods using CASTEP. *Z. Kristallogr.* **2005**, *220*, 567−570.
(31) Li, Q. A.; Gray, K. E.; Zheng, H.; Claus, H.; Rosenkranz, S.; Ancona, S. N.; Osborn, R.; Mitchell, J. F.; Chen, Y.; Lynn, J. W. Reentrant orbital order and the true ground state of $LaSr_2Mn_2O_7$. *Phys. Rev. Lett.* **2007**, *98*, 167201.
(32) Scheie, A.; Kindervater, J.; Säubert, S.; Duvinage, C.; Pfleiderer, C.; Changlani, H. J.; Zhang, S.; Harriger, L.; Arpino, K.; Koohpayeh, S. M.; Tchernyshyov, O.; Broholm, C. Reentrant phase diagram of $Yb_2Ti_2O_7$ in a <111> magnetic field. *Phys. Rev. Lett.* **2017**, *119*, 127201.
(33) Dho, J.; Kim, W. S.; Hur, N. H. Reentrant spin glass behavior in Cr-doped perovskite manganite. *Phys. Rev. Lett.* **2002**, *89*, No. 027202.
(34) Fabini, D. H.; Stoumpos, C. C.; Laurita, G.; Kaltazoglou, A.; Kontos, A. G.; Falaras, P.; Kanatzidis, M. G.; Seshadri, R. Reentrant structural and optical properties and large positive thermal expansion in perovskite formamidinium lead iodide. *Angew. Chem., Int. Ed.* **2016**, *55*, 15392−15396.
(35) Wang, Y.; Dong, X.; Tang, X.; Zheng, H.; Li, K.; Lin, X.; Fang, L.; Sun, G.; Chen, X.; Xie, L.; et al. Pressure-induced Diels-Alder reactions in C_6H_6-C_6F_6 cocrystal towards graphene structure. *Angew. Chem., Int. Ed.* **2019**, *58*, 1468−1473.
(36) Wong, H. L. S.; Allan, D. R.; Champness, N. R.; McMaster, J.; Schröder, M.; Blake, A. J. Bowing to the pressure of $\pi\cdots\pi$ interactions: Bending of phenyl rings in a palladium(II) thioether crown complex. *Angew. Chem., Int. Ed.* **2013**, *52*, 5093−5095.
(37) Paquin, R.; Limage, M. -H.; Colomban, P. Micro-Raman study of PET single fibers under high hydrostatic pressure: Phase/conformation transition and amorphization. *J. Raman Spectrosc.* **2007**, *38*, 1097−1105.
(38) Collings, I. E.; Cairns, A. B.; Thompson, A. L.; Parker, J. E.; Tang, C. C.; Tucker, M. G.; Catafesta, J.; Levelut, C.; Haines, J.; Dmitriev, V.; Pattison, P.; Goodwin, A. L. Homologous critical behavior in the molecular frameworks $Zn(CN)_2$ and Cd(imidazolate)$_2$. *J. Am. Chem. Soc.* **2013**, *135*, 7610−7620.
(39) Colombo, L.; VolovSek, V.; Furik, K.; Durig, J. R. Application of Raman spectroscopy in recognition of the two crystalline forms of terephthalic acid. *J Raman Spectrosc.* **1990**, *21*, 169−175.
(40) Syassen, K. Ruby under pressure. *High Press. Res.* **2008**, *28*, 75−126.
(41) Li, Y.; Yin, C.; Yang, X.; Kuang, X.; Chen, J.; He, L.; Ding, Q.; Zhao, S.; Hong, M.; Luo, J. A Nonlinear optical switchable sulfate of ultrawide bandgap. *CCS Chem.* **2020**, *2*, 2298−2306.
(42) Ma, Z.; Li, F.; Zhao, D.; Xiao, G.; Zou, B. Whether or not emission of Cs_4PbBr_6 nanocrystals: High-pressure experimental evidence. *CCS Chem.* **2020**, *2*, 71−80.
(43) Brik, M. G.; Srivastava, A. M. A review of the electronic structure and optical properties of ions with d^3 electron configuration (V^{2+}, Cr^{3+}, Mn^{4+}, Fe^{5+}) and main related misconceptions. *ECS J. Solid State Sci. Technol.* **2018**, *7*, 3079−3085.
(44) Eggert, J. H.; Moshary, F.; Evans, W. J.; Goettel, K. A.; Silvera, I. F. Ruby at high pressure. III. A pumping scheme for the R lines up to 230 GPa. *Phys. Rev. B* **1991**, *44*, 7202−7208.
(45) Sugano, S.; Tanabe, Y.; Kamimura, H. *Multiplets of transition-metal ions in crystals*; Academic Press Inc.: New York, US. 1970.

https://doi.org/10.1021/acs.chemmater.1c04398
Chem. Mater. 2022, 34, 2764−2770